JMEPEG (2018) 27:1694–1705
https://doi.org/10.1007/s11665-018-3276-z

1059-9495/$19.00

Effect of Different Thermomechanical Processes on the Microstructure, Texture, and Mechanical Properties of API 5L X70 Steel

Mohammad Masoumi, Edwan Anderson Ariza Echeverri, Cleiton Carvalho Silva, Miloslav Béreš, and Hamilton Ferreira Gomes de Abreu

(Submitted March 3, 2017; in revised form September 15, 2017; published online March 14, 2018)

A commercial API 5L X70 steel plate was subjected to different thermomechanical processes to propose a novel thermomechanical rolling path to achieve improved mechanical properties. Scanning electron microscopy, electron backscatter diffraction, and x-ray texture analysis were employed for microstructural characterization. The results showed that strain-free recrystallized {001} ferrite grains that developed at higher rolling temperature could not meet the American Petroleum Institute (API) requirements. Also, refined and work-hardened grains that have formed in the intercritical region with high stored energy do not provide suitable tensile properties. However, fine martensite–austenite constituents dispersed in ferrite matrix with grains having predominantly {111} and {110} orientations parallel to the normal direction that developed under isothermal rolling at 850 °C provided an outstanding combination of tensile strength and ductility.

Keywords API 5L X70 steel, crystallographic texture, thermomechanical processes

1. Introduction

American Petroleum Institute (API) steels are widely used for large-diameter pipelines to transport crude gas and oil under high pressure over long distances. Although higher grades of pipeline steels (i.e., X80 and X100) are under investigation, some difficulties such as weldability and hydrogen-induced cracking (HIC) resistance restrict the execution of these grades in long-distance pipelines (Ref 1-3). As an alternative, API 5L X70 still remains widely used in industrial pipeline application due to its easier and lower cost fabrication with more uniform mechanical properties and corrosion resistance. Thermomechanical control processing (TMCP), which refers to a multistage deformation sequence above and/or below the nonrecrystallization temperature (T_{NR}), was replaced by hot rolling and normalizing to increase the strength and toughness of pipeline steels, leading to a significant contribution to costs reductions of pipeline projects (Ref 4-6). TMCP based on temperature regions is categorized into three main types: (1) processing in the high-temperature region, or above the T_{NR}, to produce fine recrystallized austenite grains, (2) processing below the T_{NR}, to obtain pancake-shaped austenite grains with an increased number of nucleation sites for the austenite-to-ferrite transition, and (3) processing in the temperature region between A_{r3} and A_{r1}, where a mixture of austenite and ferrite exists. The ferrite is responsible for increasing the work hardening rate of the material while the austenite leads to additional hardening through the multiplication of nucleation sites for ferrite formation. The reduction of ferrite grain sizes (grain boundary strengthening), elimination of pearlite–ferrite banding, increase in density of dislocations (work hardening), and the introduction of interstitial or substitutional atoms (solid-solution strengthening) or a second phase (precipitation hardening) can significantly improve both the strength and toughness of API steels via thermomechanical rolling.

The crystallographic texture and distribution of grain boundaries developed by deformation and post-heat treatment play a significant role in the final room-temperature mechanical properties (Ref 7-9). The texture of a rolled sheet is represented by {hkl}⟨uvw⟩, in which {hkl} planes are parallel to the rolling plane and the ⟨uvw⟩ directions are parallel to the rolling direction (Ref 10). Sainath et al. (Ref 11) studied the effect of different orientations of body-centered cubic (BCC) iron on the tensile deformation and reported a meaningful difference in stress–strain response for different crystal orientations and atomic configurations. The variation in yield stress (YS) under tensile loading as a function of crystal orientation in BCC Fe was in the following order: $YS_{111} > YS_{110} > YS_{112} > YS_{100}$ (Ref 11). Herrera et al. (Ref 12) also demonstrated that the grains with {110}, {112}, and {123} planes, corresponding to most densely packed planes (slip planes) in the BCC structure, have excellent formability. On the contrary, Ghosh et al. (Ref 13) reported that cleavage {001}//ND grains provide an easy path for cracks, leading to a reduction in the mechanical properties. In addition, various researchers (Ref 14-17) showed that the presence of grains oriented with {001} parallel to the normal direction (ND), which were developed during the

Mohammad Masoumi, Department of Metallurgical and Materials Engineering, University of São Paulo, Av. Prof. Mello Moraes, 2463, São Paulo, SP CEP: 05508-030, Brazil; and Department of Metallurgical and Materials Engineering, Federal University of Ceará, Campus do Pici, 729, Fortaleza, CE CEP: 60440-554, Brazil; **Edwan Anderson Ariza Echeverri**, Department of Metallurgical and Materials Engineering, University of São Paulo, Av. Prof. Mello Moraes, 2463, São Paulo, SP CEP: 05508-030, Brazil; and **Cleiton Carvalho Silva, Miloslav Béreš,** and **Hamilton Ferreira Gomes de Abreu**, Department of Metallurgical and Materials Engineering, Federal University of Ceará, Campus do Pici, 729, Fortaleza, CE CEP: 60440-554, Brazil. Contact e-mail: mohammad.masoumi@usp.br.

recrystallization processing in the austenite region followed by ferrite transformation, have a harmful effect on hydrogen embrittlement, leading to a significant reduction in ductility.

Microstructural features such as dislocation accumulation, hardening precipitates, grain orientations, and boundary types govern the mechanical properties of steels. The control of rolling temperature at the beginning of and during deformation is critical to produce a uniform region of ultrafine equiaxed ferrite that simultaneously increases the strength, toughness, and ductility (Ref 18-20). In this paper, a commercial API 5L X70 steel was subjected to four different finish rolling temperatures by using a laboratory hot rolling mill. The effect of complex microstructure, crystallographic texture, and grain boundary characteristics on the tensile properties was investigated to propose a novel thermomechanical rolling path to achieve excellent mechanical properties by means of microstructural and textural features.

2. Experimental Procedure

A commercial API 5L X70 steel plate with a chemical composition of 0.10 C, 1.66 Mn, 0.82 Mo, and less than 0.14 wt.% micro-alloying elements Nb + Ti + V was studied in this work. The initial sample with a thickness of 9 mm was cut into four specimens (namely A, B, C, and D) in the rolling direction, and the as-received samples were heated to 1200 °C for 1 h to ensure the dissolution of inclusions and the elimination of pearlite–ferrite bands and segregation zones. Then, the samples were subjected to four different thermomechanical paths, as shown schematically in Fig. 1 [adapted from Nafisi et al. (Ref 4)]. The rolling was performed by using a laboratory rolling mill (Stanat TA-315) with a cylinder 128 mm in diameter and a rotational speed of 27 rpm. Rolling was carried out in three passes (9 mm $\rightarrow$ 7 mm $\rightarrow$ 5 mm $\rightarrow$ 2 mm) to reach a thickness of 2 mm. The contact angle was determined to be approximately 7° in accordance with the laboratory rolls; thus, the strain rates of the three passes were approximately 3.5, 4.6, and 7.8 s^{-1}, respectively. It is worth mentioning that the main purpose of using the different start and finish rolling temperatures (950-833, 860-737, 900-620 °C, and isothermally at 850 °C for samples A, B, C, and D, respectively), which were lower than the non-recrystallization temperature (T_{NR} = 1006 °C), was to obtain a similar microstructure with different crystallographic textures.

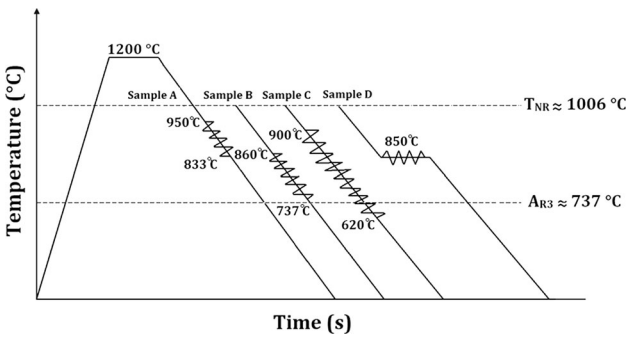

Fig. 1 Schematic representation of the thermomechanical rolling paths

Microstructural studies were carried out along the rolling direction (RD)–normal direction (ND) plane in all specimens using scanning electron microscopy (SEM, FEI Quanta FEG 450). Samples were prepared using standard metallographic procedures including grinding, mechanical polishing, and etching with Nital 2%. Vickers hardness was measured in the mid-thickness of the RD–ND plane under an indentation load of 4.903 N (0.5 kg) for 15 s ($HV_{0.5}$). Tensile tests were performed at room temperature based on the ASTM E8 M-13a standard on samples with a gauge length of 50 mm and overall length of 200 mm under a strain rate of 2×10^{-2} s^{-1}. The tensile fracture surface of each fractured tensile sample (A–D) was also investigated by SEM. Additionally, the stereology quantitative technique (Ref 21) was used to quantify the area fraction of martensite–austenite (M–A) constituents using a mesh of 483 points superimposed on the SEM microstructures.

Macrotexture measurements were taken using a Philips X-Pert diffractometer equipped with a texture goniometer. Three incomplete pole figures, that is, {110}, {200}, and {211}, were obtained, using Cu radiation, in the reflection mode on a 5° grid at a sample tilt of up to 85°. Orientation distribution functions (ODFs) of each sample were calculated from the measured pole figures using the MTEX open-source software toolbox (Ref 22). The φ_2 = 45° section of Euler space was used to display the computed ODFs.

Electron backscatter diffraction (EBSD) measurements were taken in a plane perpendicular to the transverse direction of the samples. The specimens were ground using silicon carbide paper from grade 100 to 1200, followed by polishing with diamond paste (6, 3, and 1 μm), and finally polished with 0.05 μm colloidal silica slurry for 3 h. Microtexture analyses were conducted using the Channel 5 data processing software package (Oxford Instruments®) installed on an SEM (FEI Quanta FEG 450). The backscattered electrons generated from the sample as a result of primary electron–specimen interaction project a characteristic diffraction pattern (Kikuchi pattern) following Bragg's diffraction conditions. The principles of Kikuchi pattern generation and analysis are addressed vividly in a review by Dingley and Randle (Ref 10, 23). The working distance was set to about 17 mm with a tilt angle of 70°. The accelerating voltage of the gun was adjusted to 25 kV. However, the color-coding of the EBSD map represents the crystal direction of the material within the sample reference system (i.e., X, Y, and Z). The ODF can characterize the crystallographic directions by the Euler angles $(\varphi_1, \phi, \varphi_2)$ and Miller indices (hkl) [uvw]. ODFs were estimated from EBSD maps by means of the statistical kernel density estimation method and plotted at constant Euler angles of $\varphi_2 = 45°$.

3. Results and Discussion

3.1 Microstructural Analyses

3.1.1 SEM Studies. The SEM micrographs of the investigated samples subjected to different types of TMCP are presented in Fig. 2. Ferrite as a primary microstructure in low-carbon hot-rolled API steel was developed in all TMCP samples. However, a dispersion of fine M–A constituents was

found in samples A and D, which can enhance the fracture toughness because of phase transformation. This distribution might be explained by the delayed pearlitic reaction that occurs during the continuous cooling due to the high manganese content of the studied steel. The blocky M–A constituents, or the remaining austenite coexisting with martensite, are formed under favorable conditions of chemical composition and appropriate continuous cooling rates of the untransformed carbon-enriched austenite by carbon partitioning from ferrite into the remaining austenite during austenitic decomposition (Ref 24, 25). The formation of M–A constituents could also be explained by the manganese segregation from the prior austenite to the grain boundaries during cooling, leading to an increase in the stability of austenite at room temperature. In other words, blocky austenite grains were partially transformed into martensite, forming M–A constituents. XRD analysis was carried out to show the existence of different phases in the microstructure. Although x-ray diffraction is a powerful technique for phase identification, this method has some limitations, such as detecting minority phases (at concentrations and particle sizes greater than $\approx 1\%$ and ≈ 2 μm) (Ref 26, 27). Figure 3 shows the XRD diffraction patterns of all investigated samples. Sample A, which was rolled at higher temperature, shows a significant amount of M–A constituents, or remaining austenite coexisting with martensite ($\approx 12\%$). In addition, EBSD is a useful quantitative method to confirm the presence of small particles from their diffracted Kikuchi patterns. Figure 4 shows the phase map of sample A obtained from the EBSD data, confirming the presence of fine untransformed M–A constituents, mainly at the grain boundaries. It is worth mentioning that an improvement in mechanical properties is expected of samples A and D because of the distribution of M–A constituents in the ferritic structure (Fig. 2a and d).

Figure 2(b) and (c) shows the small fraction of degenerated pearlite morphology with fragments of cementite lamellae resulted from the rolling at lower temperatures. In addition, granular bainite is identified in Fig. 2(b) and (c) and is associated with carbon-enriched secondary micro-constituents at elevated temperature (Ref 28). Samples subjected to rolling close to the A_{r3} temperature (samples B and C) were mainly composed of granular bainite with a small amount of secondary phases. However, the ferrite phase consisting of polygonal ferrite surrounded by M–A constituents is observed in Fig. 2(a) and (d). In conclusion, various microstructures (such as polygonal and elongated ferrite, granular bainite, degenerated pearlite, and M–A constituents) were characterized under different thermomechanical paths, and hence, different mechanical properties are expected.

The area fraction of M–A constituents in sample A was measured by quantitative stereology (Ref 21) (with a mesh of 483 points superimposed on the SEM microstructures) using the SEM images and by EBSD phase identification. The M–A

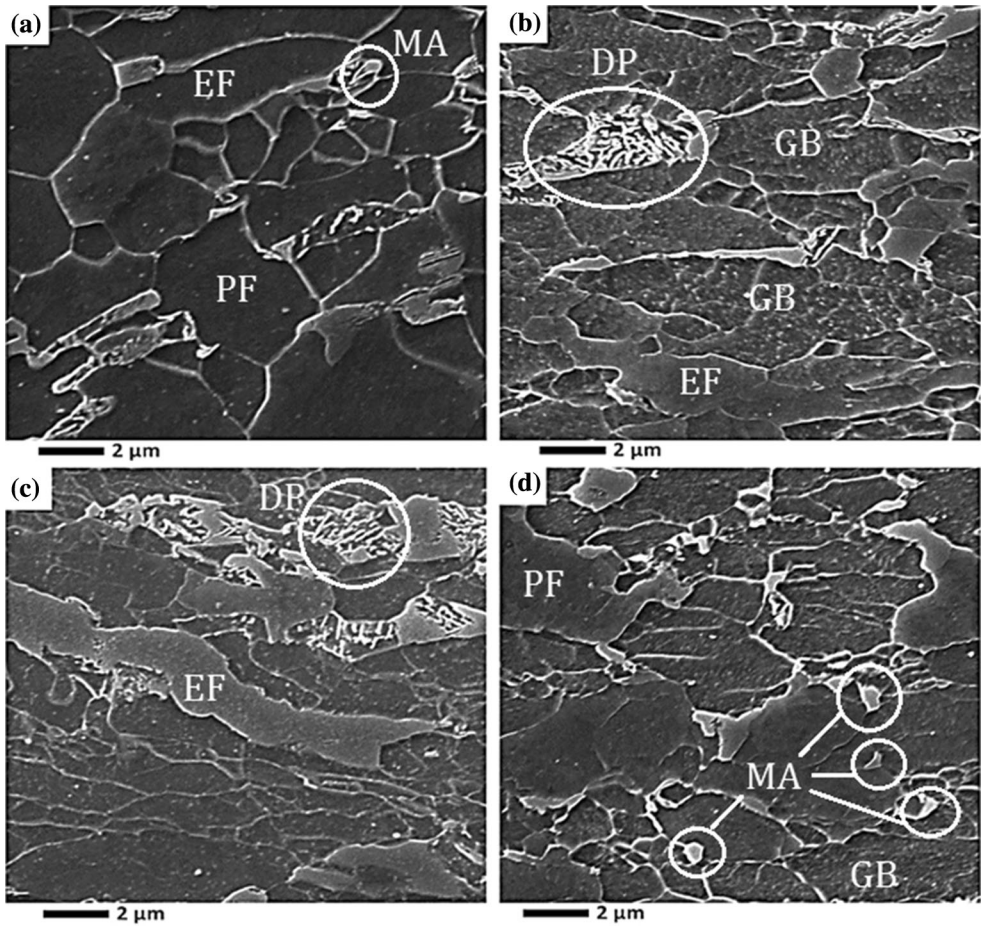

Fig. 2 SEM micrographs of samples: (a) A, (b) B, (c) C, and (d) D. PF, polygonal ferrite; EF, elongated ferrite; GB, granular bainite; DP, degenerated pearlite; MA, martensite–austenite constituents

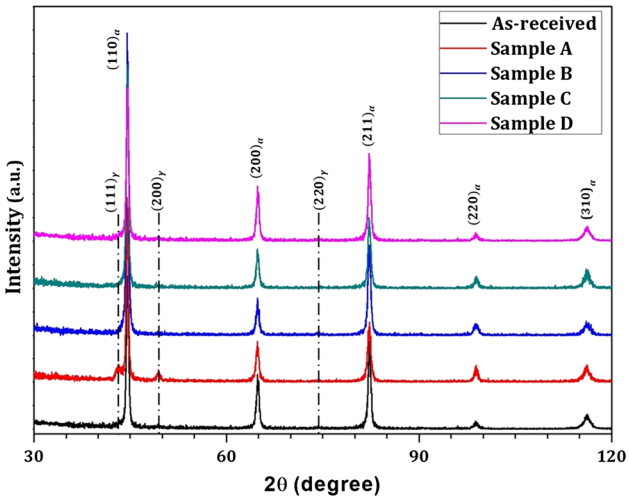

Fig. 3 XRD patterns of samples A, B, C, and D after thermomechanical processing and in as-received state, showing the normalized intensities of the ferrite (α) and remaining austenite (γ) coexisting with martensite (M–A) peaks

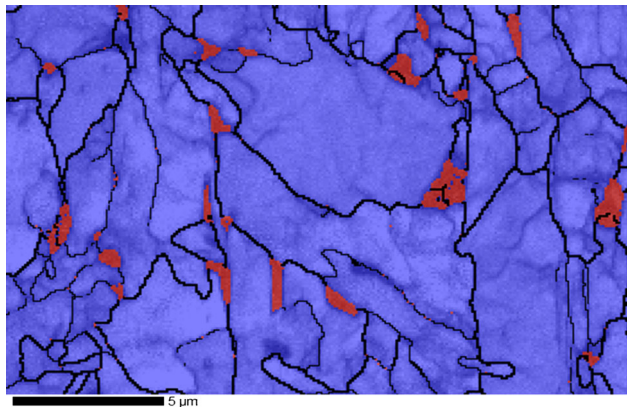

Fig. 4 Distribution of M–A constituents (red) in a polygonal ferritic matrix (blue) (Color figure online)

constituent fraction was measured as 1.5 ± 0.8 and $1.96 \pm 0.10\%$ by the stereology and EBSD techniques, respectively, and these values are much lower than the XRD result ($\approx 12\%$). There are several parameters responsible for this significant difference, such as less superficial martensite transformation by means of metallographic sample preparation, higher-penetration analysis, and a larger measured area. In addition, the penetration depth of x-rays (approximately 11 μm) is greater than that of electrons (approximately 0.05 μm) (Ref 29); thus, XRD provides more of a bulk measurement and is therefore less sensitive to surface effects (Ref 30).

Figure 5 shows the variation of average grain sizes and hardness values of samples. A significant grain size reduction was observed in all thermomechanically processed samples due to the decrease in the finish rolling temperature. This indicates that the prior austenite grain boundaries acted as preferred sites for ferrite nucleation during cooling. Thus, a high number of fine ferrite grains developed under all proposed TMCPs. Rolling in the intercritical (α + γ) region caused the development of deformed austenite and ferrite, and therefore, (1) deformed austenite (pancaked austenite grains with large boundaries) provided more ferrite nucleation, leading to final ferrite grain refinements, and (2) deformed ferrite with higher dislocation density generated by deformation is responsible for increased hardness. This could explain why the finest ferrite grain size was accompanied by the highest hardness, as observed in sample C. Furthermore, the hardness increased in all TMCP samples (except for sample A) due to the higher number of obstacles to dislocation movement caused by the increase in the fraction of grain boundaries (i.e., finest grain sizes). It is known that the applied deformation reduces the radius of the critical embryo required for dynamic recrystallization (Ref 31). Accordingly, predominantly strain-free recrystallized ferrite grains developed in sample A. Moreover, the presence of M–A constituents with lower hardness meant that this thermomechanical path led to the lowest hardness. On the contrary, samples B and C, which contained elongated ferrite, degenerated pearlite, and granular bainite, showed the highest hardness among the TMCP samples.

3.1.2 EBSD Analysis. As mentioned earlier, the EBSD technique provides comprehensive and useful quantitative data regarding the phase distribution, local grain orientation, and boundary distributions. EBSD analysis was carried out on TMCP samples to obtain better characterization and to predict the mechanical properties. Figure 6 presents the ND inverse pole figure (IPF) maps of samples A–D. Medium-angle grain boundaries (MAGBs) calculated with point-to-point misorientations of between 5° and 15° are represented by thin black lines and high-angle grain boundaries (HAGBs) with misorientations greater than 15° by thick black lines. In addition, each color indicates the specific crystal orientation related to the individual grain. For instance, red color grains indicate grains aligned with the axis {100} parallel to the ND, while blue and green colors indicate {111} and {110}//ND.

In order to characterize the change of grain orientation by different thermomechanical paths, the ODF of each set of EBSD data was calculated separately and is presented in Fig. 7. The texture components including (001)[0 $\bar{1}$0], (001)[1 $\bar{3}$0], and (001)[$\bar{1}\bar{3}$0] can be observed in Fig. 7(a) and (b). Furthermore, rolling at lower temperature eliminated the undesirable texture components. The (331)[1 $\bar{1}$0] ($\varphi_1 = 0°$, $\phi = 76°$, and $\varphi_2 = 45°$) and (110)[3 $\bar{3}$1] ($\varphi_1 = 15°$, $\phi = 90°$, and $\varphi_2 = 45°$) texture components developed at lower finish rolling temperatures in samples C and D played an important role in the improvement of mechanical properties. The rotated cube (001)[0 $\bar{1}$0] component ($\varphi_1 = 45°$, $\phi = 0°$, and $\varphi_2 = 45°$) is considered as a recrystallized rotated cube orientation, which is in accordance with the microstructural results. Recently, Sainath et al. (Ref 11) and Blondé et al. (Ref 32) reported that the increase in the Young's modulus by means of the orientation dependence on the interatomic planes is ordered as follows: $E_{(100)} < E_{(110)} < E_{(111)}$. Thus, it could be expected that samples C and D would have a greater chance of showing higher ductility corresponding the crystal orientations.

The distribution of boundary types obtained from each EBSD data result is presented in Fig. 8. The highest fraction of low-angle grain boundaries (LAGBs, point-to-point misorientation of less than 5°) among all the samples was observed in sample A, indicating that dynamic recrystallization occurred completely with this thermomechanical path. It also confirmed the reduction of recrystallization temperature by increasing the amount of deformation. Thus, a new set of strain-free recrystallized grains

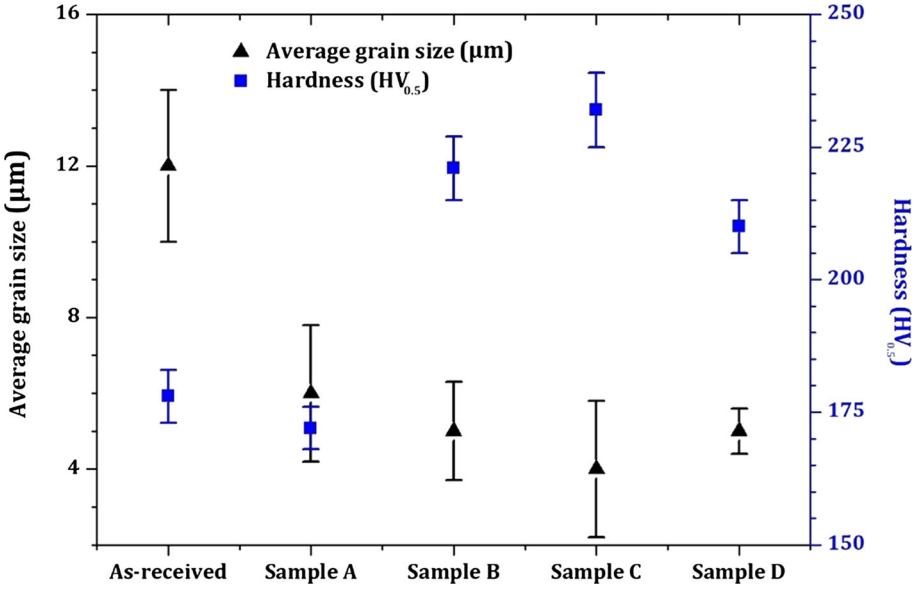

Fig. 5 Variation of average grain sizes and Vickers hardness values under a test load of 0.5 kg ($HV_{0.5}$)

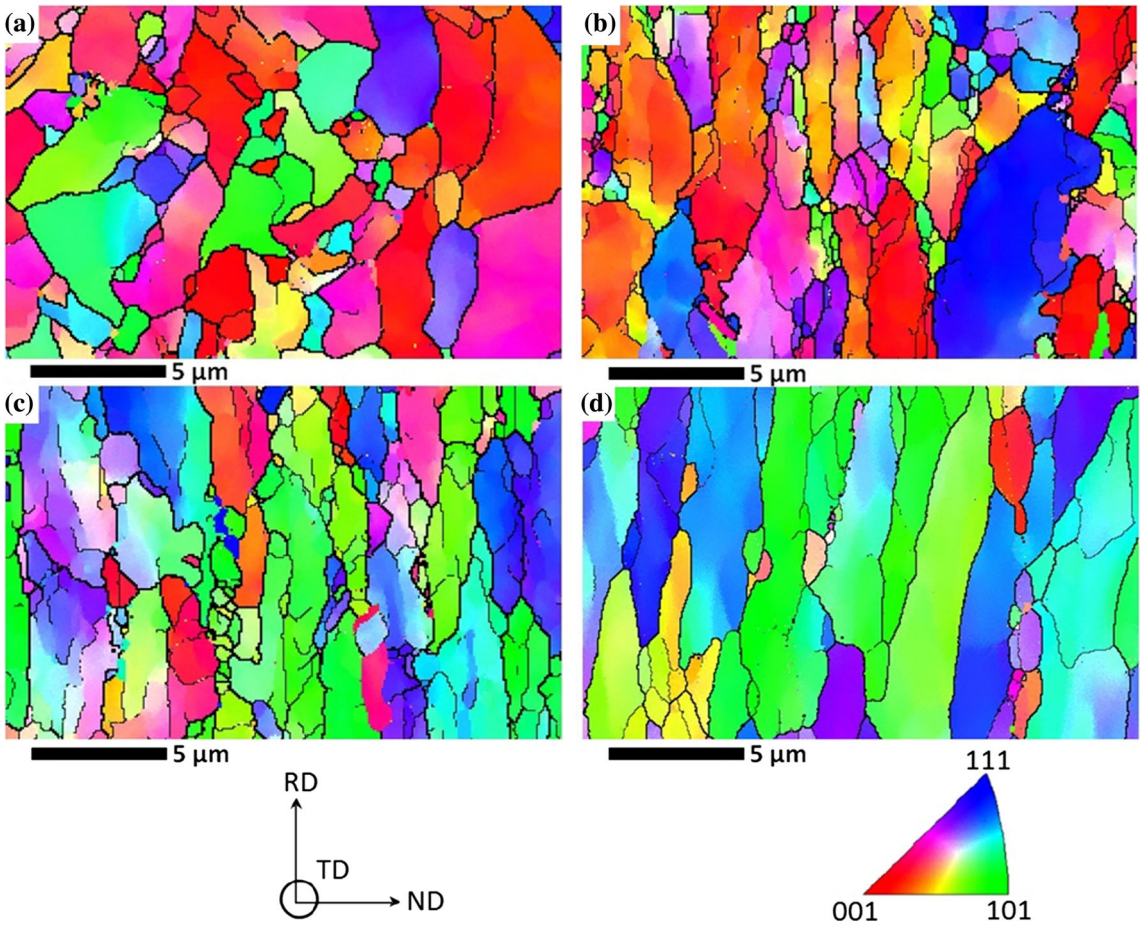

Fig. 6 The ND IPFs of TCMP samples: (a) A, (b) B, (c) C, and (d) D

were formed. However, it is notable that recrystallized grains were developed with the lowest Young's modulus. In addition, the polygonal ferrite formed in sample A (Fig. 2a) permits long-range diffusion of carbon and alloying elements to form coherent boundaries with low internal energy and a high fraction of LAGBs. On the contrary, sample C exhibited the greatest fraction of HAGBs, which is attributed to the high dislocation density during deformation at relatively low temperature. This

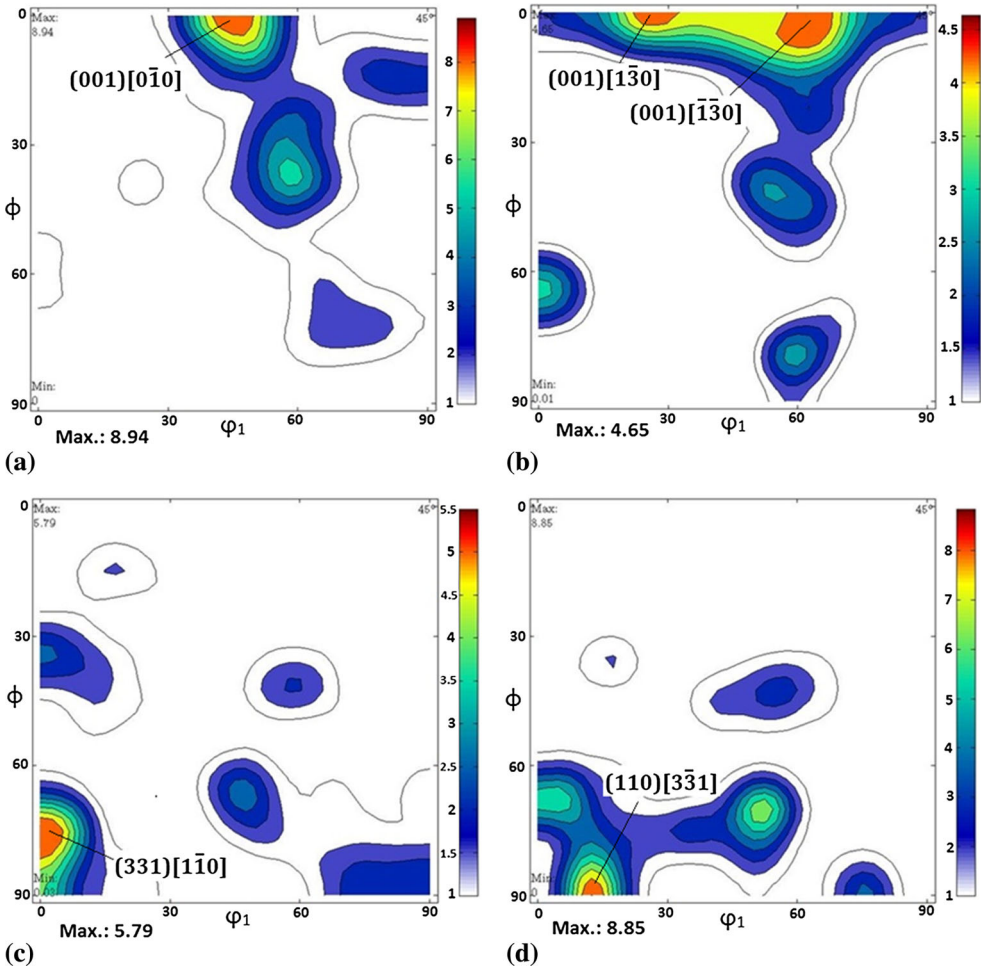

Fig. 7 ODFs at $\varphi_2 = 45°$ calculated from EBSD data (referring to Fig. 6) from TCMP samples: (a) A, (b) B, (c) C, and (d) D

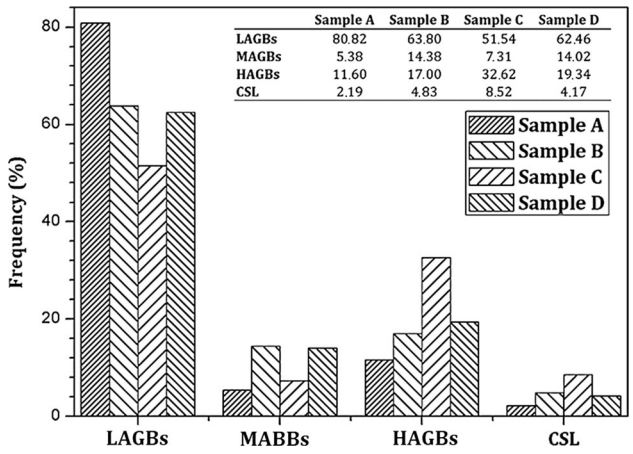

Fig. 8 Distribution of boundary types for all the TCMP samples (referring to Fig. 6)

means that dislocation generated by rolling at lower temperatures was absorbed at ferrite grain boundaries, leading to an increase in the lattice distortion. Increasing the lattice distortion (i.e., the stored energy) provides the preferred path with fewer obstacles to crack propagation. Thus, the least ductility was expected in this condition (sample C).

Coincidence site lattice (CSL) boundaries are considered as HAGBs with lower internal energy due to the specific lattice arrangements and misorientation angle (Ref 33). The fraction of CSL boundaries in sample C was more than twice as high as that in the other specimens. The detailed distribution of CSL boundaries up to Σ29 is shown in Fig. 9. It is observed that the major differences appeared at the Σ3, 17b, and 25b boundaries. Although the Σ 3^n boundaries are indicated as twin boundaries, Arafin et al. (Ref 16) reported that twinning structures cannot be created in low-carbon steel due to the high stacking-fault energy (BCC steel). Therefore, this boundary type is considered as HAGBs with internal energy, leading to a decrease in the mechanical properties. In addition, the Σ17b and 25b boundaries (associated with the ⟨221⟩ and ⟨331⟩ axes, respectively) are also predominant in sample C. In BCC structure, slip generally occurs in close-packed planes and directions. This means that these CSL boundaries cannot contribute to the dislocation movements, leading to the formation of dislocation pile-ups and facilitating crack initiation.

Furthermore, kernel average misorientation (KAM) analysis was calculated from the third nearest-neighbor kernels with a maximum misorientation of 5° (Ref 34) to represent the dislocation accumulation in an individual grain. KAM distribution maps expressing the distribution of local misorientations are also presented in Fig. 10. The smallest number of high KAM values (greater than 2.5°) was found in sample A. This

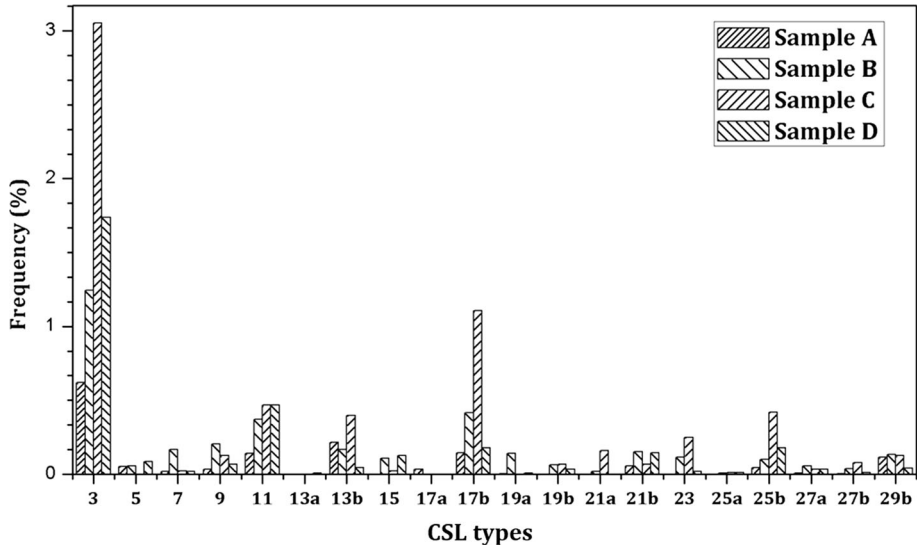

Fig. 9 Distribution of CSL boundaries in TCMP samples (referring to Fig. 6)

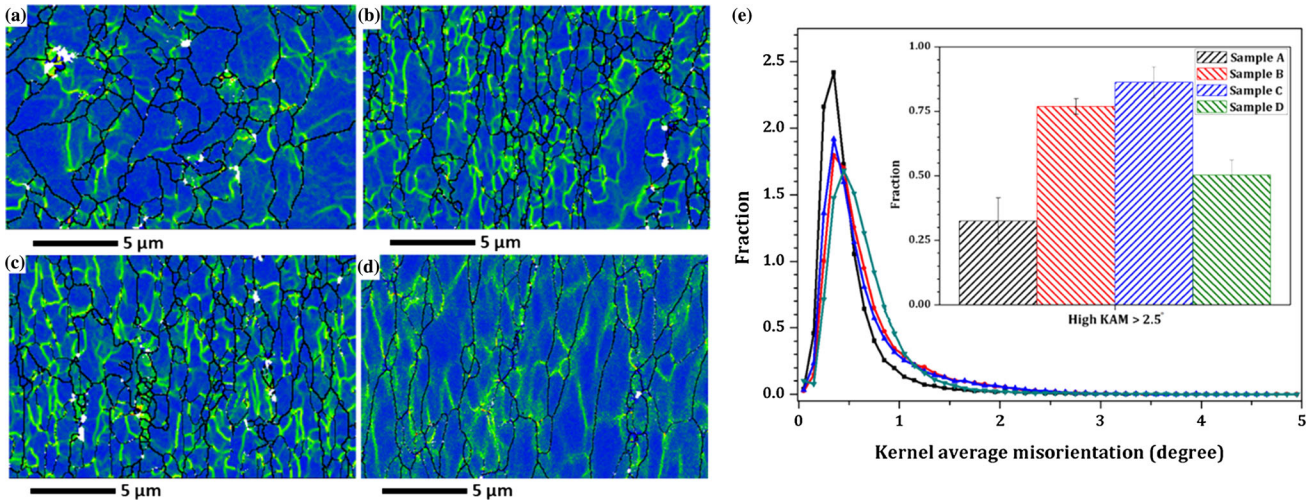

Fig. 10 (a-d) KAM distribution maps in samples A-D, respectively, and (e) values of KAM distribution (referring to Fig. 6)

could provide further confirmation of the formation of recrystallized grains in this TMCP path. By comparison, samples B and C showed high fractions of higher KAM values. This means that deformed grains developed in these thermomechanical paths, leading to a reduction in the ductility due to the higher grain distortion and stored energy. Finally, moderate KAM values were identified in sample D (rolled isothermally at 850 °C). The combination of low dislocation accumulation, stored energy, and desired grain orientation can lead to better ductility and mechanical properties in sample D, as expected.

3.2 Macrotexture X-ray Diffraction

Macrotexture x-ray diffraction analysis of TMCP sample plates with multi-grain areas was carried out. A higher x-ray penetration depth can provide better quantitative information about the crystallographic orientations of samples. Figure 11 shows the calculated ODF at constant $\varphi_2 = 45°$ in all TMCP samples. The cube (001)[$1\bar{1}0$], rotated cube (001)[$\bar{1}\bar{1}0$], and $\{001\}\langle\ \bar{1}\bar{3}0\rangle$ texture components were predominant in samples A and B. However, the small fraction of fiber textures (i.e., {112}, {111}, and {110}//ND) as the main slip planes in BCC structure is common in hot rolling. Borodin et al. (Ref 35) also reported brittle crack propagation along $\{001\}\langle 110\rangle$ grains due to high shear stress concentration on non-closed-packed {001} planes. However, the development of {111} and {110}//ND components accompanied by a reduction in {001}//ND was observed in samples C and D (Fig. 11c and d). This could be attributed to the deformation of ferrite grains in the intercritical ($\alpha + \gamma$) region (Ref 36, 37). $\{112\}\langle 1\ \bar{1}0\rangle \approx 10\mathring{}$ is also characterized as one of the main slip systems in BCC structure and was found to be dominant in sample D together with γ-fibers. In BCC metals, slip occurs in the $\langle 111\rangle$ direction on {110}, {112}, and {123} planes, and the non-planar nature of the screw dislocation core makes the slip more complex (Ref 11). Thus, grains orientated along the {110} and {112} planes can make a greater contribution to dislocation gliding and facilitate plastic deformation. Meanwhile, grains aligned on non-close-packed {001} planes with the largest interplanar spacing (or interplanar distance) avoid dislocation movements

and dislocation pile-ups, leading to early fractures (Ref 38-40). Therefore, better mechanical properties are expected in samples C and D as a result of the high number of {110}- and {112}-oriented grains accompanied by the lowest number of {001}-oriented grains.

Figure 12 shows the intensity variations of texture components along the {001}, {112}, {111}, and {110}//ND texture fibers (referring to Fig. 11). The results showed that the {001} texture components were dominant in sample A and decreased gradually in samples B–D. It was observed that the minimum {001} texture fiber with the lowest Young's modulus belonged to sample D. However, the variation of texture intensity along the {112} fiber as one of the main slip planes in BCC structure is similar in all of the TMCP samples. Sample D showed a slight increase in the intensity of the $(1\bar{1}2)[110]$ component. This means that the most favorable activated slip system was found in sample D. The same tendency was observed in Fig. 12(c) and (d), where the texture intensity of sample D was maximal in the {111} and {110} planes because close-packed planes provide an easier path for dislocation gliding, leading to more ductility in this condition. The macrotexture results are in accordance with the EBSD findings. This increases the chance of obtaining better mechanical properties in sample D due to the high fraction of {112}, {111}, and {110} grains accompanied by the minimum fraction of {001} grains with the lowest Young's modulus.

3.3 Tensile Properties and Fractography

Figure 13 shows the tensile engineering stress–strain curves obtained at room temperature. The data of the mechanical properties of the TMCP samples are listed in Table 1. The minimum acceptable yield and ultimate tensile stress (UTS) values for X70 steel are determined as 486 and 565 MPa, respectively, according to the API 5L specification (Ref 41) for pipeline application. Therefore, sample A cannot meet the specification requirements due to the development of {001} grains with a low Young's modulus. Besides, the minimum uniform elongation for the UTS was determined to be 18% (Ref 41). Thus, sample C also cannot satisfy the API specification. This could be explained by the formation of a high number of HAGBs accompanied by deformed grains with high KAM values, which restricts the straining, as expected. In sample D, the distribution of fine M–A constituents in ferrite–bainite microstructure, which is associated with predominant {110} grains along with close-packed planes with high Young's modulus and grains with low KAM value, resulted in an excellent combination of strength and elongation. Additionally, the values of toughness achieved by each TCMP sample were obtained from the areas under the stress–strain curves. It was observed (Fig. 13) that the area under the curve of sample D was much larger (24-29%) than that of samples A–C. Therefore, components thermomechanically processed through

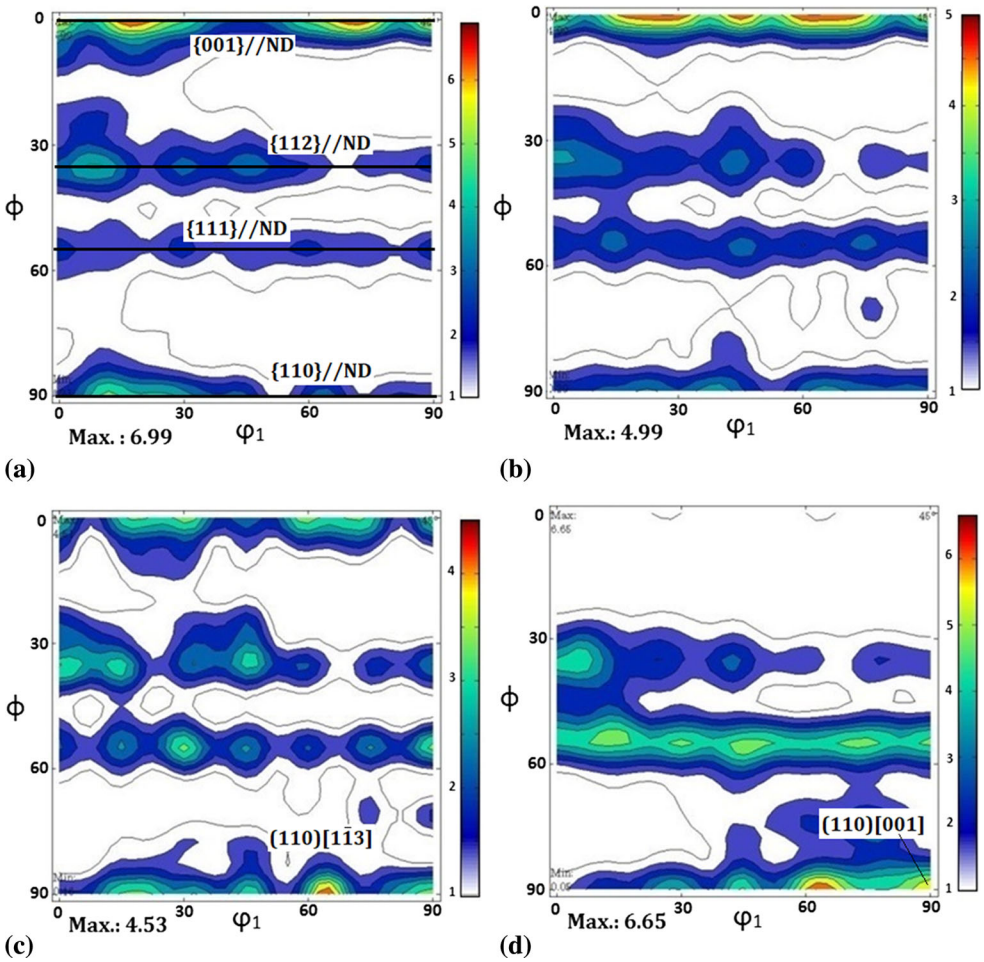

Fig. 11 Texture components in a constant $\varphi_2 = 45°$ section of the ODF of (a-d) samples A–D, respectively (referring to Fig. 1)

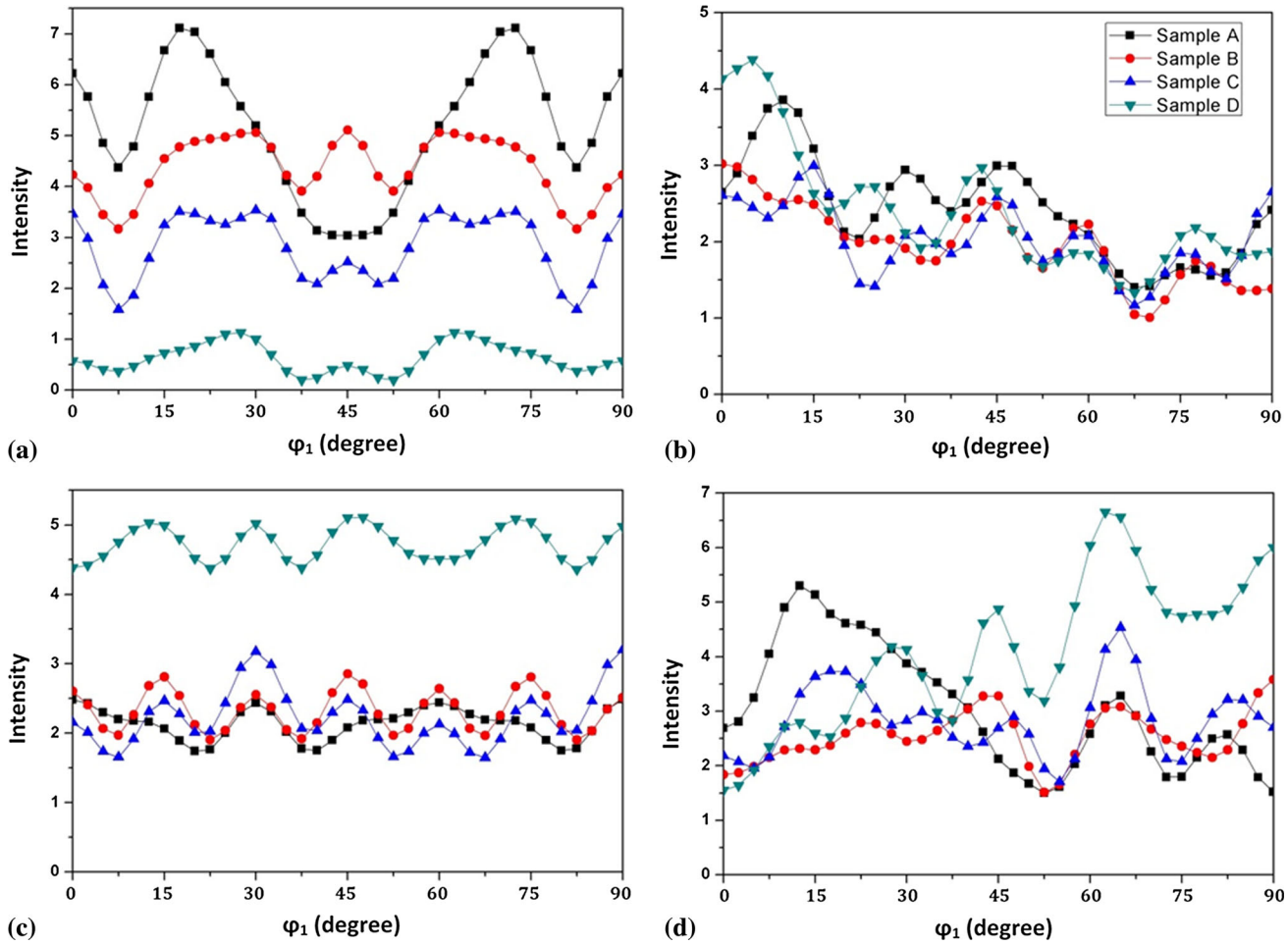

Fig. 12 Intensity variations of the texture components in TMCP samples: (a) {001}, (b) {112}, (c) {111}, and (d) {110}//ND texture fibers

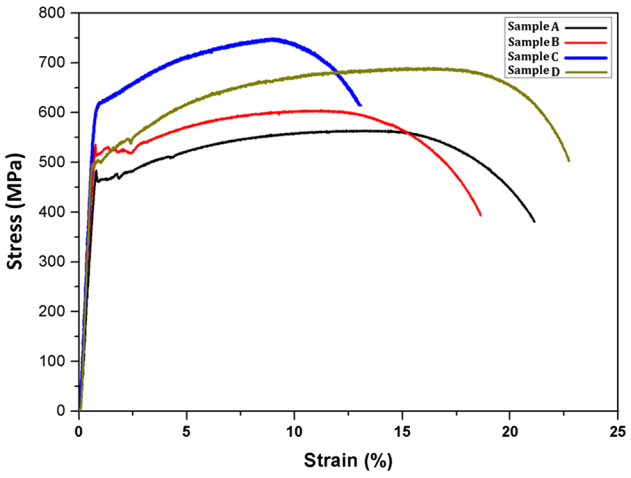

Fig. 13 Tensile engineering stress–strain curves of samples A–D

the path of sample D (see Fig. 1) could absorb more energy during impact conditions and resist the propagation of cracks.

Figure 14 shows a representative morphology from the central tensile fracture surfaces of TCMP samples A–D. In general, examination of the fracture surfaces showed cohesive tearing facets with small and large (≈ 1-10 μm) equiaxed dimples, revealing that the failure mode in all TCMP samples occurred mainly by the ductile mechanism (typical dimple ruptures). The small voids could have been caused by the failure of M–A constituents and degenerated pearlite, while larger voids could be caused by the formation of voids in ferrite. It should be noted, however, that many of the larger voids can also be composed of many smaller, shallow dimples (Ref 42). The similar fracture morphology, characterized by small-sized dimples accompanied by secondary cracks, in samples A and B (Fig. 14a and b) indicates that variations in the start temperature of rolling from 950 to 860 °C do not affect the fracture behavior significantly. The fracture surfaces observed in Fig. 14(c) and (d) also contained dimples with some flat cleavage facets joined by secondary cracks and small ductile tear ridges. The quasi-cleavage planes observed in sample C revealed the occurrence of brittle fracture mode in small local regions. Cleavage fracture is one type of transgranular cleavage, and the orientation of the cleavage facet is close to the {001} ferrite plane, which has a lower surface energy for a cleavage crack (Ref 43). Moreover, it may be the cause of the lower total elongation of sample C, as previously described. Additionally, the fracture mechanism predominantly by shearing and the many non-uniform microvoids observed in sample D indicated the high-ductility property of this sample. The increased number of dimples present in the fractures of samples A and D could be related to strain-free recrystallized grains and

Table 1 Mechanical properties determined from tensile tests of TMCP samples A–D

Sample	Yield stress, MPa	Tensile stress, MPa	Uniform elongation, %	Yield/tensile ratio	Toughness, J m^{-3}
A	462 ± 19	569 ± 23	21 ± 3	0.81	11,067
B	525 ± 16	605 ± 18	18 ± 3	0.87	10,328
C	620 ± 14	757 ± 31	13 ± 4	0.82	10,392
D	508 ± 14	690 ± 17	22 ± 3	0.73	14,361

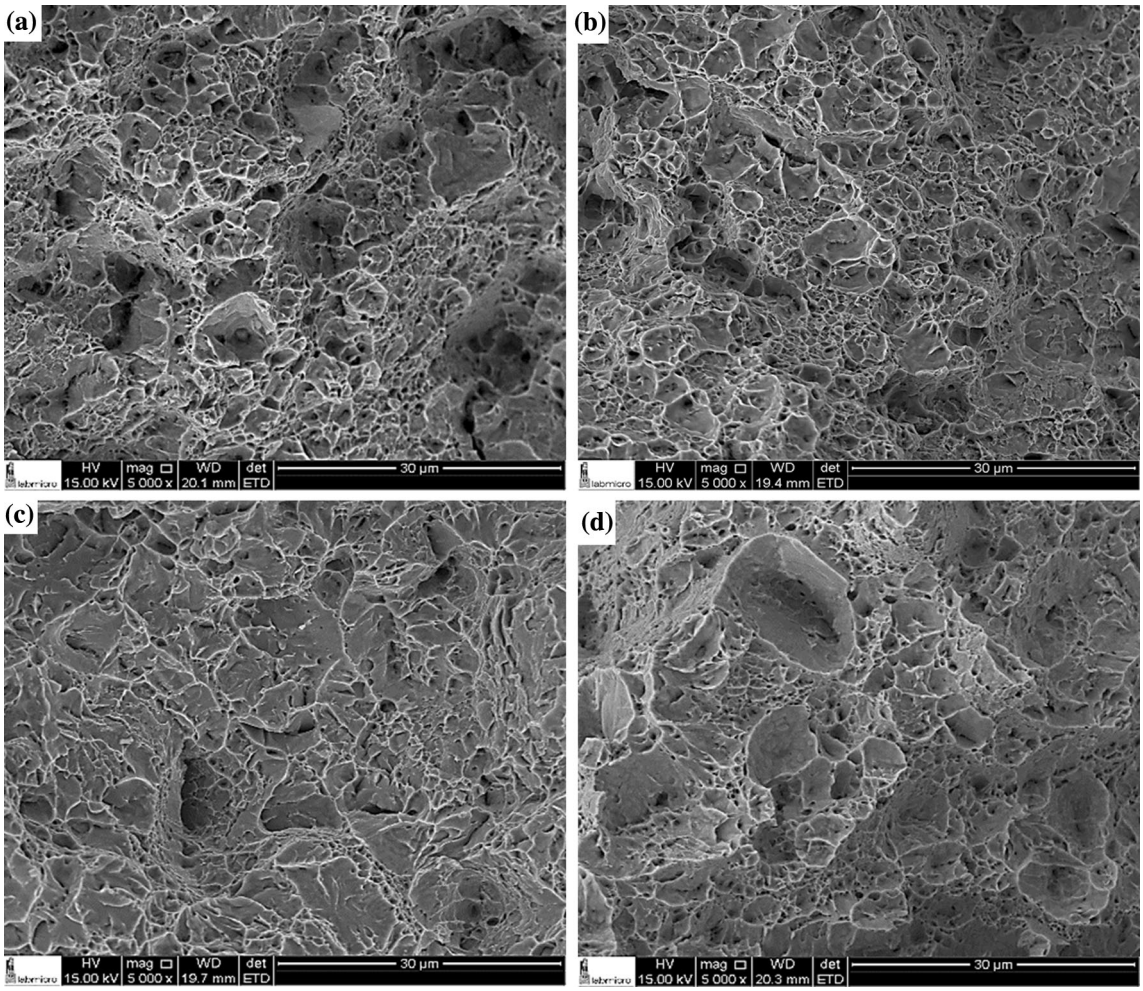

Fig. 14 SEM fractographs of TCMP samples: (a) A, (b) B, (c) C, and (d) D

the distribution of grains with low KAM values (Fig. 10e) in these samples.

The results revealed that grain orientations play a significant role in the mechanical tensile properties of API 5L X70 steel. Sainath et al. (Ref 11) and Blondé et al. (Ref 32) reported the superior Young's modulus and yield strength of grains oriented in specific densely packed crystallographic planes in BCC structure (i.e., $YS_{111} > YS_{110} > YS_{112} > YS_{100}$). On the contrary, non-close-packed {001} planes with largest interplanar distance and lack of slip systems lead to the formation of dislocation accumulation in these grains, and hence, back-stresses from the pile-ups increase. Consequently, the Griffith fracture toughness decreases and reaches a very low level in {001} grains. As a result, early fracture occurred in sample A with strain-free recrystallized {001} grains. In contrast, grains with {112}, {111}, and {110} orientations (close-packed planes in BCC crystal structure) facilitate dislocation gliding (i.e., dislocation mobility) in the BCC lattice, leading to the formation of low stored energy in sample D. Besides, the distribution of fine M–A constituents enhanced plastic deformation and improved the fracture toughness in this sample (Table 1).

4. Conclusions

The purpose of this work was to propose a novel rolling thermomechanical path to achieve improved mechanical properties by means of microstructural and textural features in a

commercial API 5L X70 steel. In accordance with the results, the following conclusions can be drawn:

1. The significant amount of M–A constituents, or remaining austenite coexisting with martensite (≈ 12%), characterized in sample A can be explained by carbon partitioning from ferrite into the remaining austenite during the austenitic decomposition and the influence of manganese segregation from the prior austenite to grain boundaries during cooling.
2. A dispersion of fine M–A constituents in the ferrite microstructure developed through the thermomechanical path of isothermal rolling at 850 °C (sample D).
3. The formation of low-KAM-value grains accompanied with low-angle boundaries could improve the tensile mechanical properties.
4. The predominance of {001} grains in sample A (non-isothermally rolled with start and finish rolling temperatures at 950 and 833 °C, respectively) is mainly responsible for the decrease in the mechanical properties.
5. The grains' predominant {111} and {110} orientations parallel to the normal direction as well as the dispersion of M–A constituents led to excellent toughness of sample D.

Acknowledgments

The authors acknowledge the CAPES and CNPq Brazilian research agencies for financial support and Central Analítica-UFC/CT-INFRA/MCTI-SISNANO/Pró-Equipamentos for providing research facilities used in this work.

References

1. K. Banerjee, Hydrogen-Induced Cold Cracking in High-Frequency Induction Welded Steel Tubes, *Metall. Mater. Trans. A*, 2016, **47**(4), p 1677–1685
2. X. Liang and A.J. Deardo, A Study of the Influence of Thermomechanical Controlled Processing on the Microstructure of Bainite in High Strength Plate Steel, *Metall. Mater. Trans. A*, 2014, **45**(11), p 5173–5184
3. S.Y. Shin, B. Hwang, S. Lee, N.J. Kim, and S.S. Ahn, Correlation of Microstructure and Charpy Impact Properties in API, X70 and X80 Line-Pipe Steels, *Mater. Sci. Eng. A*, 2007, **458**(1–2), p 281–289
4. S. Nafisi, M.A. Arafin, L. Collins, and J. Szpunar, Texture and Mechanical Properties of API, X100 Steel Manufactured Under Various Thermomechanical Cycles, *Mater. Sci. Eng. A*, 2012, **531**, p 2–11
5. H.K. Sung et al., Correlation Between Microstructures and Tensile Properties of Strain-Based API, X60 Pipeline Steels, *Metall. Mater. Trans. A*, 2016, **47**(6), p 2726–2738
6. H.K. Sung et al., Effects of Finish Cooling Temperature on Tensile Properties After Thermal Aging of Strain-Based API, X60 Linepipe Steels, *Metall. Mater. Trans. A*, 2015, **46**(9), p 3989–3998
7. K. Huang and R.E. Logé, A Review of Dynamic Recrystallization Phenomena in Metallic Materials, *Mater. Des.*, 2016, **111**, p 548–574
8. M. Masoumi, C.C. Silva, H. Ferreira, and G. De Abreu, Effect of Rolling in the Recrystallization Temperature Region Associated with a Post-Heat Treatment on the Microstructure, Crystal Orientation, and Mechanical Properties of API, 5L X70 Pipeline Steel, *Mater. Res.*, 2017, **20**(1), p 151–160
9. A. Gourgues, H.M. Flower, and T.C. Lindley, Electron Backscattering Diffraction Study of Acicular Ferrite, Bainite, and Martensite Steel Microstructures, *Mater. Sci. Technol.*, 2000, **16**, p 26–40
10. V.R.D.J. Dingley and K.Z. Baba-Kishi, *Atlas of Backscattering Kikuchi Diffraction Patterns*, Microscopy in Materials Science Series Institute of Physics Publishing, Philadelphia, 1995, p 299–306
11. G. Sainath and B.K. Choudhary, Orientation Dependent Deformation Behaviour of BCC Iron Nanowires, *Comput. Mater. Sci.*, 2016, **111**, p 406–415
12. C. Herrera, N.B. Lima, A.F. Filho, R.L. Plaut, and A.F. Padilha, Texture and Mechanical Properties Evolution of a Deep Drawing Medium Carbon Steel During Cold Rolling and Subsequent Recrystallization, *J. Mater. Process. Technol.*, 2009, **209**, p 3518–3524
13. A. Ghosh, S. Kundu, and D. Chakrabarti, Effect of Crystallographic Texture on the Cleavage Fracture Mechanism and Effective Grain Size of Ferritic Steel, *Scr. Mater.*, 2014, **81**, p 8–11
14. V. Venegas, F. Caleyo, J.M. Hallen, T. Baudin, and R. Penelle, Role of Crystallographic Texture in Hydrogen-Induced Cracking of Low Carbon Steels for Sour Service Piping, *Metall. Mater. Trans. A*, 2007, **38**, p 1022–1031
15. V. Venegas, F. Caleyo, T. Baudin, J.H. Espina-Hernández, and J.M. Hallen, On the Role of Crystallographic Texture in Mitigating Hydrogen-Induced Cracking in Pipeline Steels, *Corros. Sci.*, 2011, **53**, p 4204–4212
16. M.A. Arafin and J.A. Szpunar, A New Understanding of Intergranular Stress Corrosion Cracking Resistance of Pipeline Steel Through Grain Boundary Character and Crystallographic Texture Studies, *Corros. Sci.*, 2009, **51**, p 119–128
17. M.A. Mohtadi-Bonab, R. Karimdadashi, M. Eskandari, and J.A. Szpunar, Hydrogen-Induced Cracking Assessment in Pipeline Steels Through Permeation and Crystallographic Texture Measurements, *J. Mater. Eng. Perform.*, 2016, **25**, p 1781–1793
18. B. Mirzakhani, M.T. Salehi, S. Khoddam, S.H. Seyedein, and M.R. Aboutalebi, Investigation of Dynamic and Static Recrystallization Behavior During Thermomechanical Processing in a API-X70 Microalloyed Steel, *J. Mater. Eng. Perform.*, 2009, **18**, p 1029–1034
19. S.Y. Shin, K.J. Woo, B. Hwang, S. Kim, and S. Lee, Fracture-Toughness Analysis in Transition-Temperature Region of Three American Petroleum Institute X70 and X80 Pipeline Steels, *Metall. Mater. Trans. A*, 2009, **40**, p 867–876
20. E. El-Danaf, M. Baig, A. Almajid, W. Alshalfan, M. Al-Mojil, and S. Al-Shahrani, Mechanical, Microstructure and Texture Characterization of API, X65 Steel, *Mater. Des.*, 2013, **47**, p 529–538
21. A. 562-02, *Standard Test Method for Determining Volume Fraction by Systematic Manual Point Count* (ASTM, 2002)
22. F. Bachmann, R. Hielscher, and H. Schaeben, Ultramicroscopy Grain Detection from 2d and 3d EBSD Data—Specification of the MTEX Algorithm, *Ultramicroscopy*, 2011, **111**, p 1720–1733
23. D.A. Hughes, High Angle Boundaries Formed by Grain Subdivision Mechanisms, *Acta Mater.*, 1997, **45**, p 3871–3886
24. J.H. Yang, Q.Y. Liu, D.B. Sun, and X.Y. Li, Microstructure and Transformation Characteristics of Acicular Ferrite in High Niobium-Bearing Microalloyed Steel, *J. Iron Steel Res. Int.*, 2010, **17**(6), p 53–59
25. R.D.A. Silva, L.F.G. Souza, E.V. Morales, P.R. Rios, and I.D.S. Bott, Formation of Microphases and Constituents from Remaining Austenite Decomposition in API, X80 Steel Under Different Processing Conditions, *Mater. Res.*, 2015, **18**(5), p 908–917
26. E. Tsl and E. South, Phase Differentiation via Combined EBSD and XEDS, *J. Microsc.*, 2004, **213**, p 296–305
27. S.J.S. Qazi, A.R. Rennie, J.K. Cockcroft, and M. Vickers, Use of Wide-Angle X-ray Diffraction to Measure Shape and Size of Dispersed Colloidal Particles, *J. Colloid Interface Sci.*, 2009, **338**, p 105–110
28. P. Cizek, B.P. Wynne, C.H.J. Davies, B.C. Muddle, and P.D. Hodgson, Effect of Composition and Austenite Deformation on the Transformation Characteristics of Low-Carbon and Ultralow-Carbon Microalloyed Steels, *Metall. Mater. Trans. A*, 2002, **33**, p 1331–1349
29. J.B. Seol, D. Raabe, P.P. Choi, Y.R. Im, and C.G. Park, Atomic Scale Effects of Alloying, Partitioning, Solute Drag and Austempering on the Mechanical Properties of High-Carbon Bainitic-Austenitic TRIP Steels, *Acta Mater.*, 2012, **60**(17), p 6183–6199
30. G. Thomas, J. Speer, D. Matlock, and J. Michael, Application of Electron Backscatter Diffraction Techniques to Quenched and Partitioned Steels, *Microsc. Microanal.*, 2011, **17**(3), p 368–373
31. F.J. Humphreys, and M. Hatherly, The deformed state, in *Recrystallization and Related Annealing Phenomena*, 2 edn. (Elsevier, Oxford, 2004), pp. 11–65

32. R. Blonde et al., High-Resolution X-ray Diffraction Investigation on the Evolution of the Substructure of Individual Austenite Grains in TRIP Steels During Tensile Deformation, *Mater. Sci. Eng. A*, 2014, **47**(3), p 965–973
33. P.J. Konijnenberg, S. Zaefferer, and D. Raabe, Acta Materialia Assessment of Geometrically Necessary Dislocation Levels Derived by 3D EBSD, *Acta Mater.*, 2015, **99**, p 402–414
34. S.I. Wright, M.M. Nowell, S.P. Lindeman, P.P. Camus, M. De Graef, and M.A. Jackson, Ultramicroscopy Introduction and Comparison of New EBSD Post-Processing Methodologies, *Ultramicrosc. J.*, 2015, **159**, p 81–94
35. V.A. Borodin, P.V. Vladimirov, and A. Möslang, The Effects of Temperature on (001)⟨110⟩ crack propagation in bcc iron, *J. Nucl. Mater.*, 2013, **442**(1), p 612–617
36. M. Eskandari, A. Zarei-Hanzaki, J.A. Szpunar, M.A. Mohtadi-Bonab, A.R. Kamali, and M. Nazarian-Samani, Microstructure Evolution and Mechanical Behavior of a New Microalloyed High Mn Austenitic Steel During Compressive Deformation, *Mater. Sci. Eng. A*, 2014, **615**, p 424–435
37. M. Eskandari, M.A. Mohtadi-Bonab, and J.A. Szpunar, Evolution of the Microstructure and Texture of X70 Pipeline Steel During Cold-Rolling and Annealing Treatments, *Mater. Des.*, 2016, **90**, p 618–627
38. M.J. Serenelli, M.A. Bertinetti, and J.W. Signorelli, Investigation of the Dislocation Slip Assumption on Formability of BCC Sheet Metals, *Int. J. Mech. Sci.*, 2010, **52**, p 1723–1734
39. L. Dezerald, D. Rodney, E. Clouet, L. Ventelon, and F. Willaime, Plastic Anisotropy and Dislocation Trajectory in BCC Metals, *Nat. Commun.*, 2016, **7**, p 11695
40. J. Wang, A. Misra, R.G. Hoagland, and J.P. Hirth, Slip Transmission Across FCC/BCC Interfaces with Varying Interface Shear Strengths, *Acta Mater.*, 2012, **60**, p 1503–1513
41. API 5L, Specification for Line Pipe, vol. 42 (American Petroleum Institute, 2000), p. 153
42. W.-S. Lee and T.-T. Su, Mechanical Properties and Microstructural Features of AISI, 4340 High-Strength Alloy Steel Under Quenched and Tempered Conditions, *J. Mater. Process. Technol.*, 1999, **87**(1–3), p 198–206
43. M.Y. Tu, C.A. Hsu, W.H. Wang, and Y.F. Hsu, Comparison of Microstructure and Mechanical Behavior of Lower Bainite and Tempered Martensite in JIS SK5 Steel, *Mater. Chem. Phys.*, 2008, **107**(2–3), p 418–425